

# From One-Dimensional Disordered Racemate to Ordered Racemic Conglomerates through Metal-Coordination-Driven Self-Assembly at the Liquid-Solid Interface

Tianze Hu<sup>+</sup>,<sup>[a]</sup> Andrea Minoia<sup>+</sup>,<sup>[b]</sup> Gangamallaiiah Velpula,<sup>\*[a]</sup> Kanykei Ryskulova,<sup>[c]</sup> Kristof Van Hecke,<sup>[d]</sup> Roberto Lazzaroni,<sup>[b]</sup> Kunal S. Mali,<sup>[a]</sup> Richard Hoogenboom,<sup>[c]</sup> and Steven De Feyter<sup>\*[a]</sup>

In recent years, there has been significant focus on investigating and controlling chiral self-assembly, specifically in the context of enantiomeric separation. This study explores the self-assembly behavior of 4-dodecyl-3,6-di(2-pyridyl)pyridazine (DPP-C12) at the interface between heptanoic acid (HA) and highly oriented pyrolytic graphite (HOPG) using a combination of scanning tunneling microscopy (STM) and multiscale molecular modeling. The self-assembled monolayer structure formed

by DPP-C12 is periodic in one direction, but aperiodic in the direction orthogonal to it. These structures resemble 1D disordered racemic compounds. Upon introducing palladium [Pd(II)] ions, complexing with DPP-C12, these 1D disordered racemic compounds spontaneously transform into 2D racemic conglomerates, which is rationalized with the assistance of force-field simulations. Our findings provide insights into the regulation of two-dimensional chirality.

## Introduction

Surface confined ordered self-assembled molecular networks (SAMNs) play an important role in the fabrication of functional surfaces.<sup>[1]</sup> They found use in various applications such as energy conversion and storage,<sup>[2]</sup> catalysis,<sup>[3]</sup> and sensing<sup>[4]</sup> to name a few. The bottom-up approach has been widely explored for fabricating well-ordered SAMNs using non-covalent interactions.<sup>[1a,5]</sup> In recent years, the fabrication of metal-organic coordination networks (MOCNs) has been explored.<sup>[6]</sup> MOCNs are materials with exceptional structural versatility. They consist of metal ions interconnected by organic ligands to form

intricate crystalline structures at the nanoscale. Various organic ligands such as pyridines,<sup>[6a]</sup> carbonitriles<sup>[7]</sup> and carboxylates<sup>[8]</sup> have been used in combination with different metal ions. Their ability to precisely tailor these networks at the nanoscale enables the development of advanced materials with exceptional performance across a wide range of applications, such as catalysis, gas adsorption, drug delivery, sensing and sustainable energy solutions.<sup>[9]</sup>

Various techniques have been widely used to characterize MOCNs. For example, X-ray crystallography has been employed to determine the precise three-dimensional arrangement of atoms within the MOCN structure. Powder X-ray diffraction (PXRD) confirms crystallinity and phase purity. Spectroscopic techniques like nuclear magnetic resonance (NMR) and infrared (IR) spectroscopy provide information about chemical bonding and ligand coordination. Furthermore, nanoscale characterization of metal coordination networks provides insights into the types of interactions and orientations between metal ions and ligands. This understanding helps tailor the stability and reactivity of the network. Additionally, the orientation and arrangement of metal centers and ligands at the nanoscale influence the network's structural and physicochemical properties. Scanning probe microscopy, particularly scanning tunneling microscopy (STM), has been widely used to characterize MOCNs at the nanoscale as well. Despite the challenges associated with imaging in the presence of metal ions in solution, STM has emerged as an indispensable tool for studying the structural aspects of these networks at the nanometer scale. Because of the well-defined environmental control, most of these studies are performed under ultra-high vacuum (UHV) conditions.<sup>[6c,10]</sup> There are only few reports of MOCNs constructed and characterized at the solution-solid interface.<sup>[6a,b,11]</sup> This is because, fabricating MOCNs is relatively difficult due to the compatibility between the organic ligands and metal ions.


[a] T. Hu,<sup>+</sup> Dr. G. Velpula, Dr. K. S. Mali, Prof. S. De Feyter  
 KU Leuven, Division of Molecular Imaging and Photonics  
 Department of Chemistry  
 Celestijnenlaan 200F, 3001 Leuven (Belgium)  
 E-mail: gm.velpula@kuleuven.be  
 steven.defeyter@kuleuven.be

[b] Dr. A. Minoia,<sup>+</sup> Prof. R. Lazzaroni  
 Laboratory for Chemistry of Novel Materials  
 Materials Research Institute  
 University of Mons  
 Place du Parc 20, 7000 Mons (Belgium)

[c] Prof. Dr. K. Ryskulova, Prof. Dr. R. Hoogenboom  
 Supramolecular Chemistry Group  
 Centre of Macromolecular Chemistry  
 Department of Organic and Macromolecular Chemistry  
 Ghent University  
 Krijgslaan 281 S4, 9000, Ghent (Belgium)

[d] Prof. Dr. K. Van Hecke  
 XStruct, Department of Chemistry  
 Ghent University  
 Krijgslaan 281 S3, 9000, Ghent (Belgium)

[<sup>+</sup>] These authors contributed equally to this work.

 Supporting information for this article is available on the WWW under <https://doi.org/10.1002/chem.202302545>

In addition, controlling the morphology of the resulting network can also be a significant challenge.<sup>[12]</sup> Despite the challenges associated with fabricating and characterizing metal-organic coordination networks at solution-solid interfaces, a few of MOCNs have been developed and characterized using STM.<sup>[6a,b, 11a]</sup> These networks are typically sustained by a combination of weaker non-covalent interactions (van der Waals interactions and hydrogen bonds) and stronger coordination bonds.<sup>[6a,b]</sup>

An intriguing structural aspect of SAMNs is their chirality. Because of the surface confinement, in fact, the footprint of achiral and asymmetric molecules can become chiral. When chirality is involved, molecules can crystallize as racemic compounds or racemic conglomerates or solid solutions in two-dimensional (2D) systems.<sup>[12–13]</sup> In a 2D racemic compound, both enantiomers co-crystallize in equal amounts, resulting in periodic and achiral structures. In contrast, a 2D racemic conglomerate is composed of enantiomerically pure domains that are not intermixed. A 2D solid solution contains a random mixture of enantiomers that do not segregate into separate domains.<sup>[12–13]</sup> There exists a special and rarely reported structure known as a 1D disordered racemate based on the difference in the degree of order in molecular packing between racemates and random solid solutions.<sup>[13a,14]</sup> This structure is characterized by chiral molecules arranged periodically in one direction with a handedness, but without long-range order in the arrangement of the two enantiomers along the perpendicular direction. The exploration of chiral MOCNs has implications for various fields such as catalysis, sensing, separation as well as drug development and design.<sup>[12]</sup> Understanding surface chirality contributes to the fundamental insights into the mechanism of expression, induction, and amplification of chirality. While such chirality aspects have been well-explored for MOCNs<sup>[6c,10b]</sup> under ultrahigh vacuum (UHV) and for metal free SAMNs at the solution-solid interface,<sup>[15]</sup> there exists only a single report,<sup>[6a]</sup> describing the 2D chirality of MOCNs fabricated and characterized at the solution-solid interface.

Recently, we studied the expression and amplification of chirality in hybrid 2D metallosupramolecular networks formed by a guanine derivative appended with a pyridyl node at the solution-HOPG interface.<sup>[6a]</sup> In the absence of palladium (Pd) ions, the guanine derivative formed a racemic compound, i.e. the unit cell is composed of both enantiomers at the solution-HOPG interface. However, the system converted into a conglomerate, where multiple enantiomerically pure domains are formed at the same interface upon addition of Pd(II) ions.<sup>[6a]</sup>

In this work, we explore the transformation of an aperiodic SAMN into a periodic SAMN formed by a pyridazine derivative using a combination of STM measurements, quantum chemistry calculations and classical atomistic models. Here, a 4-dodecyl-3,6-di(2-pyridyl)pyridazine (DPP-C12) molecule (Figure 1) was synthesized by an inverse-electron demand Diels-Alder reaction<sup>[16]</sup> between 3,6-di(2-pyridyl) tetrazine and 1-tetradecyne. DPP-C12 is achiral but has an asymmetric substitution pattern leading to a chiral adsorption motive (labelled as DPP-C12+ and DPP-C12-, Figure 1b and 1c). The self-assembly of DPP-C12, was studied at the heptanoic acid (HA)/graphite

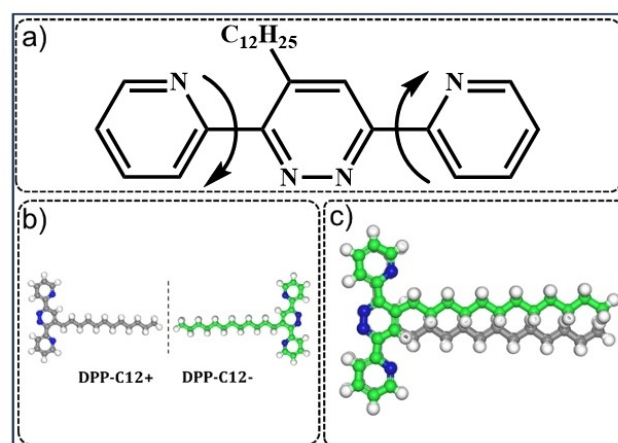


**Figure 1.** (a) DPP-C12 molecular structure, in the  $(\alpha, \beta) = (180^\circ, 180^\circ)$  conformation. Upon adsorption on a surface DPP-C12 forms a chiral entity. (b) The mirror image adsorption enantiomers DPP-C12 labelled, DPP-C12+ and DPP-C12-. For the sake of clarity, the C–C bonds have been colored in gray (green) in the DPP-C12+ (DPP-C12-) enantiomers. (c) Superimposition of DPP-C12+ and DPP-C12-.

interface. The DPP-C12 shows a packing motif, that is periodic in the direction along the molecular stacks, but aperiodic in the direction orthogonal to them. However, it was found that in the presence of palladium ions [Pd(II)], DPP-C12 forms periodic MOCNs. More importantly, we discuss the expression of chirality at the level of the dimer, the tetramer, and the monolayer. We also report how the system undergoes changes in its chiral nature upon addition of Pd(II) ions. The SAMNs correspond to a 1D disordered racemic compound in the absence of Pd(II) ions, but it transforms into a 2D racemic conglomerate upon addition of Pd(II) ions. Possible reasons behind the transformation from 1D disordered racemic compound into 2D racemic conglomerate are discussed in the light of a multiscale molecular modeling strategy.

## Results and Discussion

The experimental details for the synthesis and characterization as well as the single crystal 3D structure of DPP-C12 are included in the Supporting Information. The chemical structure of the DPP-C12 molecule is shown in Figure 1a. The two interring N–C–N torsions in the DPP-C12 core, namely  $\alpha$  and  $\beta$ , play a crucial role in the adsorption geometry of the molecule as well as in the structure of the metal-coordinated dimers. Because of the asymmetry introduced by the presence of the alkyl group, the two torsions are expected to have a different energy profile. This was calculated and confirmed by computing those torsional profiles with density functional theory (DFT) (Figure S1, Supporting Information). To reduce the energetic noise and the computational cost of the torsional scan, the dodecyl group has been replaced by a methyl group (see Supporting Information).

## Conformational Study of DPP-C12 on the HOPG surface

In order to reveal the preferred adsorption conformation of DPP-C12 on HOPG, four possible planar conformations have been considered, namely  $(\alpha,\beta) = (0^\circ,0^\circ)$ ,  $(\alpha,\beta) = (180^\circ,0^\circ)$ ,  $(\alpha,\beta) = (0^\circ,180^\circ)$ , and  $(\alpha,\beta) = (180^\circ,180^\circ)$ . These conformations have been optimized at the DFT level of theory and the resulting optimized torsional angles and relative stabilities are reported in Table S1, showing that DPP-C12 adsorbs flat on HOPG and the most stable conformation is the one having  $(\alpha,\beta) = (180^\circ,180^\circ)$  (Figure S2, Supporting Information). For the most stable conformer, the nitrogen atoms of the pyridine moiety are lying opposite to the nitrogen atoms of the pyridazine ring thereby minimizing the repulsion between the free electron pairs of the nitrogen atoms, which is similar to the molecular conformation observed in the crystal structure (Table S2, and Figure S3a, Supporting Information).

## Self-Assembly of DPP-C12

Figure 2a and Figure S4 show a well-extended supramolecular network formed by DPP-C12 at the heptanoic acid-HOPG interface. The STM image shows alternating bright columns and dark troughs. We ascribe the bright features of the columns to the pyridine units linked to the pyridazine core, whereas darker troughs correspond to the interdigitated dodecyl chains attached to the pyridazine moiety. When the orientation of the alkyl chains on both sides of the bright columns is parallel, the DPP-C12 cores are aligned parallel as well (*Type 1*, Figure 2c-top). This *Type 1* structure coincides with the single-crystal 3D structure (Figure S2b, Supporting Information). However, when the orientation of the alkyl chains on both sides of the bright columns are not parallel, one of the DPP-C12 cores is rotated by  $65^\circ$  with respect to the neighboring DPP-C12 core and forms a *Type 2* structure (Figure 2c-bottom). Both *Type 1* and *Type 2*

structures co-exist at the heptanoic acid/HOPG interface and are mixed within the SAMNs.

## Self-Assembly of DPP-C12: Periodic? or Aperiodic?

To find out whether the DPP-C12 SAMN is periodic at a larger length scale, the bright columnar structures were labelled based on the orientation of the DPP-C12 cores (Figure 3a). The bright columns formed by *Type 1* (or *Type 2*) orientation of DPP-C12 cores are labelled as 1 (or 2 or 2'). The distinction between 2 and 2' reflects the two different orientations of the alkyl chains of the *Type 2* packing (see Figure 3a). A corresponding molecular model is shown in Figure 3c. It clearly reveals the relationship between the orientation of the alkyl side chains and the interactions between the DPP-C12 cores. The sequence 212' 222' 111 2'21 2'2 in Figure 3b and 3d indicates that the SAMN of DPP-C12 is aperiodic, and any apparent periodicity, such as the one 122' 122' 122' observed locally (Figure 3a and Figure 3c), is just a coincidence. It should be noted that the aperiodicity of the DPP-C12 SAMNs is not concentration-dependent and persists even upon annealing the samples at  $80^\circ\text{C}$ .

To evaluate the relative abundance of *Type 1* or *Type 2* motifs, the sequence of the bright columns in 45 individual STM images was analyzed (927 rows in total). These images are obtained on different samples and in different experimental sessions. The probability of finding the two orientations is 54% for *Type 1* and 46% for *Type 2*, with large image-to-image variations, the cumulative weighted average value reaching a plateau. As kinetics factors may contribute as well, the result is in line with the stabilization energies calculated for both structures. A detailed discussion is provided in the modeling section.

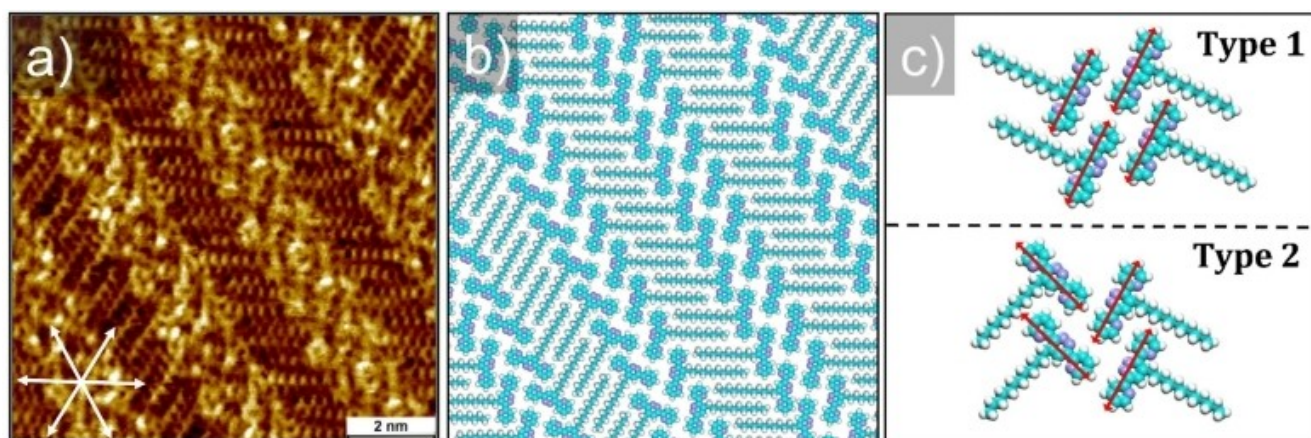


**Figure 2.** (a) High-resolution STM image of the adlayer formed by DPP-C12 at the heptanoic acid (HA)/HOPG interface ( $C_{\text{DPP-C12}} = 1.0 \times 10^{-3}$  M). Graphite symmetry axes are indicated in the lower left corner. Imaging parameters:  $I_{\text{set}} = 150$  pA,  $V_{\text{bias}} = -600$  mV. (b) Molecular models corresponding to the STM images provided in (a). (c) Two types of packing structures formed by DPP-C12.

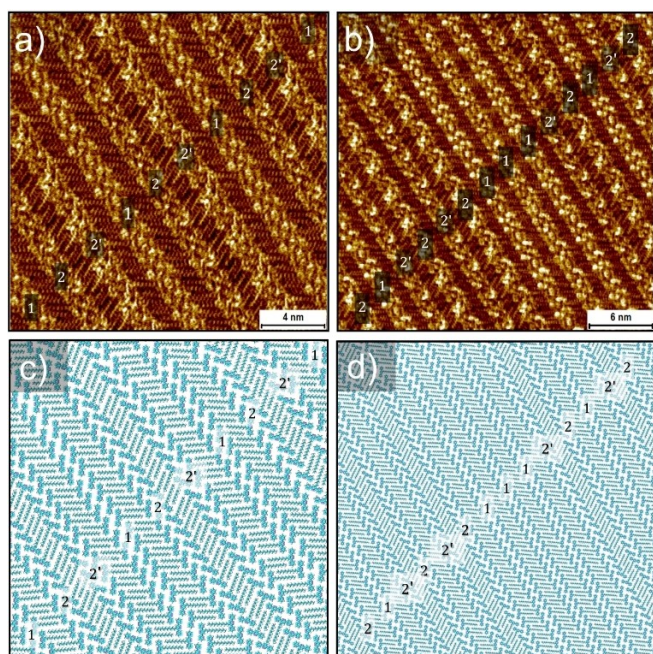


**Figure 3.** (a and b) High-resolution STM images of the adlayer formed by DPP-C12 at the HA/HOPG interface. 1, 2 and 2' labels are used to distinguish the orientation of DPP-C12 molecules. (c and d) Molecular models corresponding to the STM images provided in a and b, respectively. parameters: (a)  $I_{\text{set}} = 70$  pA,  $V_{\text{bias}} = -820$  mV. (b)  $I_{\text{set}} = 150$  pA,  $V_{\text{bias}} = -600$  mV.

## Mechanism Behind the Aperiodicity of DPP-C12 Self-assembly and Chirality

To gain insight into the mechanism underlying the formation of aperiodic SAMNs of DPP-C12, we computed and compared the stability of various DPP-C12 aggregates, namely dimers and tetramers and these results are summarized in Figure 4.

### From DPP-C12 Dimers to Tetramers

#### Pairing of DPP-C12 via Cores

In order to establish how the molecules prefer to assemble once adsorbed on HOPG, we compare the stability of dimers in which molecules pair up either via their cores (C) or via their alkyl tails (A). At first, we consider how DPP-C12 molecules can interact by pairing their cores. Two molecular orientations have been considered, one where the cores are parallel (Figure 4, C1) and the other where the cores are tilted at about  $65^\circ$  (Figure 4, C2). Those two dimers are representative of the *Type 1* and *Type 2* core orientations observed in the STM image (Figure 2a), and their stability on surface is  $-54.6$  kcal/mol and  $-50.9$  kcal/mol, respectively. While the C1- and C2- dimers are homochiral, their heterochiral counterparts i.e., C3- and C4-dimers have comparable stability, as the interactions between the DPP-C12 cores are the same (Figure 4, C3 and Figure 4, C4).

Pairing via Cores			Pairing via Alkyl-Chains				
Type	Dimers model	Energy (kcal/mol)	Dimers model	Energy (kcal/mol)	From dimer to tetramers	Tetramers model	Energy (kcal/mol)
Homochiral	C1 Type-1	-54.6	A1 Homochiral	-63.9		T1	-133.1
	C2 Type-2	-50.9	A2	-62.8		T2	-136.7
Heterochiral	C3 Type-1	-54.6	A3 Heterochiral	-62.6		T3	-134.1
	C4 Type-2	-50.9	A4	-61.9	T4	-133.9	

**Figure 4.** Chirality and geometry of DPP-C12 dimers and tetramers with molecules adsorbed in different conformations and interacting via different modes (pairing via cores and pairing via alkyl chains). DPP-C12 dimers and tetramers are also shown in the Supporting Information (Figure S5, S6 and S7). The DPP-C12+ and DPP-C12- enantiomers are shown in different colors.

### Pairing of DPP-C12 via Alkyl Chains

Dimers can also be formed when the molecules are pairing via their alkyl tails. Due to the asymmetric nature of the DPP-C12 core and the resulting molecular prochirality, four inequivalent types of dimers can be identified (Figure 4, A1-4). These dimers are 8–10 kcal/mol more stable than those shown in Figure 4, C1-4, with the most stable dimer of all (–63.9 kcal/mol) being the one shown in Figure 4, A1. These results indicate that the formation of the monolayer is dominated by the interactions between the DPP-C12 alkyl tails, rather than by specific interactions between the DPP-C12 cores. Of the four possible dimers, the first two (Figure 4, A1-2) are homochiral dimers, while the other two (Figure 4, A3-4) are heterochiral dimers. To evaluate how these dimers can grow into the columns of interdigitated alkyl groups as observed experimentally, we studied how molecules can organize in small aggregates of two interacting dimers.

### Aggregates of Two Interacting Dimers

Interestingly, the aggregate formed by the most stable dimer (the A1 dimer) is the least stable of all, being about 3.3 kcal/mol higher in energy than the most stable aggregate, which is the one formed by the A2 dimer as shown in the Figure 4, A2. This is due to the overall rectangular shape of the A1 dimer which prevents the perfect interdigitation of the alkyl groups, so that a gap appears in between the dimers (Figure 4, T1). Instead, the A2 dimer, which was only 1.1 kcal/mol less stable than the A1 dimer is now the most favorable building block for constructing DPP-C12 aggregates, as its shape promotes a favorable interdigitation between the alkyl chains, which results in formation of compact and ordered aggregates. Aggregates from the heterochiral dimers A3 and A4 are shown in (Figure 4, T3,4) and are about 2.6–2.8 kcal/mol more energetic than the most stable system.

### DPP-C12 assembly on graphite: From Tetramers to Monolayer

In order to understand the observed aperiodicity in the DPP-C12 monolayer, we then modeled how two molecular aggregates can interact. At first, homochiral seeds composed of two interacting T2 aggregates are created in the *Type 1* and *Type 2* orientation (Figure 5a and Figure 5c, respectively) and then they are extended to build longer stacks. It appears clearly that a *Type 1* homochiral seed (Figure 5a) can be propagated to form a *Type 1* structure (Figure 5b). In stark contrast a *Type 2* homochiral seed (Figure 5c) cannot be used to create *Type 2* structures (Figure 5d). A similar analysis can be carried out assembling heterochiral seed; *Type 2* heterochiral seeds (Figure 6a) can interact to form

extended *Type 2* structures (Figure 6b) but *Type 1* heterochiral seeds (Figure 6c) cannot form *Type 1* structures (Figure 6d).

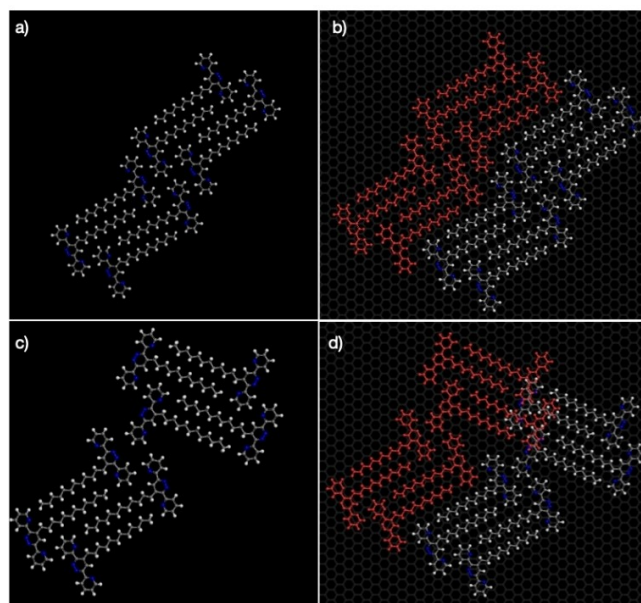


**Figure 5.** (a) *Type 1* homochiral seed and (b) the resulting *Type 1* homochiral structure. (c) *Type 2* homochiral seed and (d) the resulting *Type 2* homochiral structure. Molecules in red are in the replicated seed.

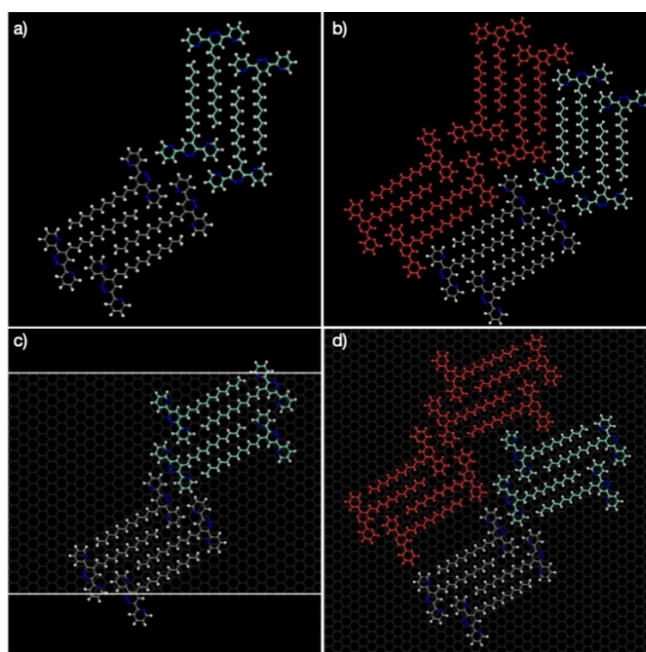


**Figure 6.** (a) *Type 2* heterochiral seed and (b) the resulting *Type 2* heterochiral structure. (c) *Type 1* heterochiral seed and (d) the resulting *Type 1* heterochiral structure. Molecules in red are in the replicated seed and DPP-C12- enantiomers are shown.

It is worth noting that regardless of the type of structure formed, individual molecular stacks are always enantiopure structures, being created by the assembly of either the DPP-C12+ or the DPP-C12- enantiomers. Since DPP-C12 molecules do not have a preferential adsorption orientation on graphite, stacks of DPP-C12+ and DPP-C12- enantiomers are both expected to form on the surface. These findings suggest that

*Type 1* and *Type 2* structures can be seen as the two possible types of interfaces between homochiral stacks: when the interacting enantiopure stacks have the same chirality, they form a *Type 1* structure and when the interacting stacks have opposite chirality, then their interface is a *Type 2* structure. This concept is illustrated in

Figure 7, where the DPP-C12 molecules on either side of the red dashed line show the same stacking structure, but their chirality is different. The SAMNs formed by these stacks do not obey the definition of racemic compounds<sup>[17]</sup> due to their aperiodic nature. In addition, they also do not belong to the solid solution<sup>[18]</sup> as they are periodic in one direction. Instead, they are a rare type of 1D disordered racemates.<sup>[13a,14, 19]</sup> This structure is characterized by having the chiral molecules arranged into 1D periodic homochiral stacks that are randomly mixed in the monolayer, thus making the overall structure aperiodic.

To understand the factors contributing to the formation of 1D disordered racemates, we conducted calculations to determine the relative stability of the two interfaces. Our analysis revealed that the homochiral *seed* (taken as ideal model for *Type 1* interfaces) is only 1.6 kcal/mol more stable than the heterochiral one (taken as ideal model for the *Type 2* interface). This slight difference in the stability clearly: (i) accounts for the similar experimental relative abundance of *Type 1* vs *Type 2* interfaces (54% vs 46%) in the monolayer and (ii) makes it entropically favorable to randomly mix stacks of opposite chirality rather than creating few extended homochiral domains like those found in a typical racemic conglomerate. Furthermore, the interactions between molecules within the stacks are found to be stronger than those between adjacent homo (or hetero) chiral stacks. We hypothesize that the aperiodic monolayer is the result of the joining of enantiopure stacks (homochiral '+' domains and heterochiral '-' domains) (see Figure 7) as they grow and diffuse on the surface, creating a relatively weak interface whose geometry depends on the chirality of the interacting stacks.

This systematic study on the interaction between the DPP-C12 molecules to form monolayers clearly explains the origin of

aperiodicity and role of chirality in the DPP-C12 SAMNs. These networks are stabilized by dominant van der Waals interactions prevailing between the alkyl chains within a row and weak non-directional interactions between the DPP-C12 cores. Note that DPP-C12 is prochiral, leading to two mirror-image motifs. The compound forms homo- and heterochiral stacks. Interaction between the homochiral stacks leads to the formation of the *Type 1* interface, whereas heterochiral stacks direct the formation of the *Type 2* interface. Both chiral stacks have similar stabilization energies. Therefore, they randomly come in contact and form 1D disordered racemates.

### Coordination-Driven DPP-C12 Self-Assembly

In the absence of metal ions, DPP-C12 forms an aperiodic 1D disordered racemic SAMNs mainly sustained by van der Waals interactions between interdigitated alkyl chains rather than the interactions between the DPP-C12 cores. It is well known that metal ions form adducts with Lewis's base ligands such as pyridine groups. Therefore, we explored the possibility of regulating the interactions between the cores of the DPP-C12 molecules by metal ion complexation and therefore to affect the self-assembly behavior, with a particular interest to the chirality of the resulting MOCNs. Palladium chloride (PdCl<sub>2</sub>) was selected because it forms coordinate complexes with a large range of ligands including pyridine. Firstly, PdCl<sub>2</sub> was dissolved in dimethyl sulfoxide (DMSO) and diluted with heptanoic acid. Then a PdCl<sub>2</sub>/DMSO/HA mixture (0.5 mM, DMSO/HA = 1:19) was added to the DPP-C12 solution in HA to form a 2:1 mixture of the ligand and the metal. In contrast to the aperiodic SAMNs obtained without Pd(II), deposition of such a pre-mixed metal-ligand solution yielded highly ordered MOCNs (Figure 8a, Figure S8, Supporting Information) at the HA/HOPG interface. Furthermore, identical MOCNs of the DPP-C12/Pd(II) complex have also been observed when PdCl<sub>2</sub> was added in situ to the HOPG substrate containing already formed aperiodic SAMNs of DPP-C12 (Figure S9, Supporting Information). This indicates the dynamic behavior of the system under the experimental conditions.

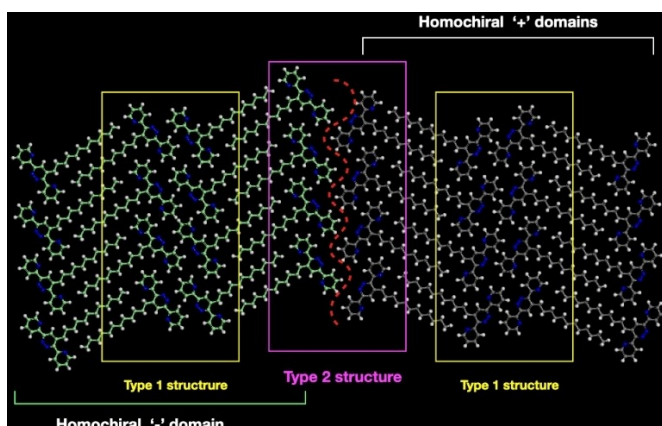


**Figure 7.** *Type 1* interfaces are found in homochiral domains, while *Type 2* interfaces are formed when stacks of opposite chirality come into contact.

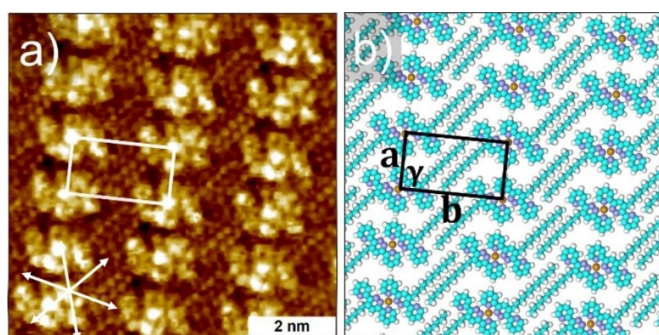


**Figure 8.** Self-assembly of DPP-C12 at the HA/HOPG interface in the presence of Pd(II) ions ( $C_{\text{DPP-C12}} = 1.0 \times 10^{-3}$  M,  $C_{\text{PdCl}_2} = 5 \times 10^{-4}$  M). (a) Small-scale, high-resolution STM images of the adlayer formed by the DPP-C12/Pd molecules at the same interface. Imaging parameters:  $I_{\text{set}} = 30$  pA,  $V_{\text{bias}} = -820$  mV.

The relative orientation of the **DPP-C12** cores as well as the alignment of alkyl chains within the columns is uniform. This significant change in the network and peculiar STM contrast at the anticipated metal-ligand junction indicates successful coordination of **DPP-C12** to Pd(II) ions. The unit cell parameters for the MOCNs of the **DPP-C12/Pd(II)** complex are  $a=1.5 \pm 0.1$  nm,  $b=2.6 \pm 0.1$  nm, and  $\gamma=89 \pm 1^\circ$  (Figure 8b). Each unit cell contains two **DPP-C12** molecules and one Pd(II) ion. The molecular density is 0.51 molecules/nm<sup>2</sup>. It is worth noting that the molecular density is 0.66 molecules/nm<sup>2</sup> in the absence of Pd(II) ions, and the adjacent **DPP-C12** molecules along the columns are tightly packed and the distance between the molecules is shorter ( $1.3 \pm 0.1$  nm). Upon the addition of Pd(II) ions, the intermolecular distance between adjacent molecules slightly increases, resulting in a 23% decrease in the molecular density.

**DPP-C12** has multiple metal coordinate sites and is capable of complexing more than one metal center.<sup>[20]</sup> It has been reported that metal-complexed pyridazine derivatives may appear as two different conformers. For  $\alpha=180^\circ$  and  $\beta=0^\circ$ , two **DPP-C12** molecules bind to one metal atom. In case of the most unstable adsorption conformation in absence of metal ions,  $\alpha=0^\circ$  and  $\beta=0^\circ$  (Table S1, Supporting Information), two **DPP** molecules link with two metal atoms.<sup>[20]</sup> The STM images, however, provide clear evidence for the formation of the metal-ligand complexes. A bright spot is present in between two **DPP-C12** molecules (Figure 8a), where two **DPP-C12** molecules bind to one Pd(II) ion. A molecular model based on calibrated STM data is shown in Figure 8b.

### From **DPP-C12/Pd(II)** Dimers to Monolayers and Chirality

The structure of isolated mono-coordinated dimers has been investigated by means of theoretical calculations and the results are shown in Figure S10 in the Supporting Information. The most stable structure is the one in which both **DPP-C12** molecules are in a  $\alpha=180^\circ$  and  $\beta=0^\circ$  conformation. Note that since the most stable conformation of non-metalated **DPP-C12** adsorption ( $\alpha=180^\circ$  and  $\beta=180^\circ$ ) is not suitable for metal coordination, the theoretical results suggest metal coordination is most likely to occur with the molecules that are in solution rather than with those already adsorbed on HOPG. To test this idea, UV-vis spectra of both **DPP-C12** and **DPP-C12/Pd(II)** in solution have been recorded (Figure S11, Supporting Information). Both **DPP-C12** and **DPP-C12/Pd(II)** show absorption bands at 238 nm ( $\pi-\pi^*$ ) and 287 nm ( $n-\pi^*$ ). A significant increase in the intensity of the absorption band at 238 nm ( $\pi-\pi^*$ ) is observed upon addition of Pd(II) ions to the **DPP-C12** solution. The enhancement in this absorption band is due to the coordination interactions between the Pd(II) ions and **DPP-C12**. Therefore, both the experimental and theoretical findings support the hypothesis that metal-coordination already takes place in solution.

Several monolayers have been modeled with the most stable coordinated dimer and the most promising resulting

structure is shown in Figure S12 in the Supporting Information. This modelled

monolayer not only quantitatively matches the STM images but its unit cell ( $a=1.3 \pm 0.1$  nm,  $b=2.6 \pm 0.1$  nm, and  $\gamma=88 \pm 1^\circ$ ) is in a good quantitative agreement with the experimental one ( $a=1.5 \pm 0.1$  nm,  $b=2.6 \pm 0.1$  nm, and  $\gamma=89 \pm 1^\circ$ ). It is important to note here that similar to the **DPP-C12 dimers**, **DPP-C12/Pd(II)** dimers are also prochiral (Figure 8a), and do not present any preferential adsorption sides. Therefore, both the dimer B+ and dimer B- enantiomers are expected to be present on the surface (see Figure 9b, Figure S13). Since the model that best fits the experimental data is a homochiral domain, i.e. only composed of B+ or B- dimers homochiral domains of opposite chirality should be observed. Indeed, large-scale STM images (Figure 9b) show that multiple enantiopure domains of opposite chirality coexist at the solution-HOPG interface. This confirms the validity of our theoretical model and it indicates that the MOCNs formed by **DPP-C12** in the presence of Pd(II) are racemic conglomerates. Conglomerate crystallization is an important step for the separation of two enantiomers in the bulk.<sup>[21]</sup> Recently, we have explored such metal-ion mediated spontaneous resolution for the guanine derivative appended with an ethynyl-4-pyridyl moiety (**C6G-4Py**).<sup>[6a]</sup>

To understand the formation of racemic conglomerates of **DPP-C12/Pd(II)** MOCNs, we conducted theoretical calculations and analyzed monolayers formed by **DPP-C12/Pd(II)** units (Figure S12, Supporting Information). The formation of the racemic conglomerate is mainly driven by a combination of coordination interactions, between the **DPP-C12** cores and Pd(II) ions, as well as van der Waals interactions between the interdigitated alkyl chains on both sides of the **DPP-C12/Pd(II)** dimers. These interactions collectively control the orientation of the molecules in the MOCNs.

The **DPP-C12/Pd(II)** complex forms periodic MOCNs, unlike **DPP-C12** SAMNs. The periodic nature of **DPP-C12/Pd(II)** is due to the fact that the metal-coordinated dimers have two alkyl groups that cannot pair together and are oriented along the same direction (with a small offset). This orientation of alkyl chains is defined by a combination of relatively stronger metal-coordinated interactions between **DPP-C12** and Pd(II) and the overall geometry of **DPP-C12/Pd(II)** dimers. Furthermore, the

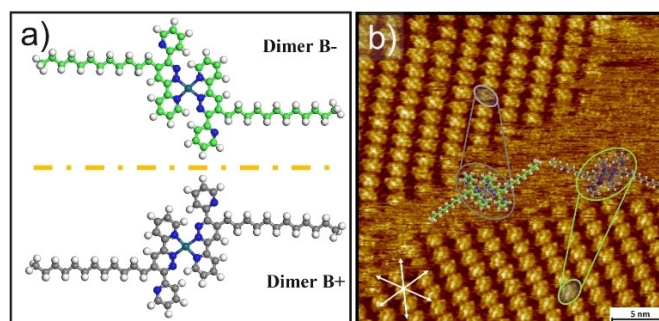


**Figure 9.** (a) Prochiral metal-coordinated dimer. (b) Large-scale STM image shows two domains. The chirality of the molecules in both the domains is represented by the dimers B+ (gray) and B- (green) enantiomers. Imaging parameters:  $I_{set} = 110$  pA,  $V_{bias} = -600$  mV.

adjacent dimers interdigitate their alkyl groups in a specific way leading to the formation of highly ordered extended monolayers.

Like **DPP-C12** dimers, metal-coordinated dimers are also prochiral. However, because of the strict way the dimers can interact, only large homochiral domains are found, indicating the formation of a racemic conglomerate on the surface.

## Conclusions

This study demonstrates a molecular-level understanding of the transformation from a 1D disordered racemate **DPP-C12** SAMN into a 2D racemic conglomerate **DPP-C12/Pd(II)** MOCN at the solution-solid interface. We provide mechanistic insights into this transformation at the level of “dimers” using high-resolution STM data, as well as atomistic models and quantum calculations. These reveal that the formation of 1D disordered racemate **DPP-C12** SAMNs is due to **DPP-C12** prochirality and the dominance of intrarow interactions, driven by the tendency of the molecules to interact through pairing their alkyl chains, which results in enantiopure stack growth. Since there are no specific interactions between the **DPP-C12** cores, the stacks can interact in two different favorable ways, the inter-row interactions being nearly isoenergetic. This makes it entropically favorable for the stacks to randomly mix, resulting in 1D disordered racemates.

However, the addition of Pd(II) ions enhances the interactions between the **DPP-C12** conjugated cores, further controlling the interactions between the **DPP-C12/Pd(II)** dimers through interdigitation of the alkyl chains. The way the dimers interact leads to the formation of large homochiral domains, resulting in the formation of a racemic conglomerate on the surface.

Overall, this study emphasizes the role of coordination interactions in controlling the order and chirality of metal-organic coordination networks, providing valuable insights into the recognition and regulation of two-dimensional chirality.

## Experimental Section

### Scanning tunneling microscopy (STM)

A stock solution of **DPP-C12** ( $C_{\text{DPP-C12}} = 1.0 \times 10^{-3}$  M) was prepared by dissolving the appropriate amount of solid in 1-heptanoic acid (HA) (Sigma-Aldrich  $\geq 99\%$ ). The stock solution was diluted further with HA to make a concentration series. The stock solution of palladium chloride ( $\text{PdCl}_2$ ) (Sigma-Aldrich) was prepared by dissolving  $\text{PdCl}_2$  in dimethyl sulfoxide (DMSO) ( $C_{\text{DMSO}} = 1.0 \times 10^{-2}$  M). The stock solutions were diluted further with HA to make a concentration series. A 2:1 mole ratio of **DPP-C12** and  $\text{PdCl}_2$  mixture was prepared by mixing the appropriate volumes of **DPP-C12** and  $\text{PdCl}_2$  solutions. All STM experiments were performed at room temperature (21–23 °C) using a PicoLE (Agilent) machine operating in constant-current mode with the tip immersed in the supernatant liquid. STM tips were prepared by mechanically cutting a Pt/Ir wire (80%/20%, diameter 0.2 mm). Prior to imaging, a drop of solution was placed onto a freshly cleaved surface of highly oriented

pyrolytic graphite (HOPG, grade ZYB, Advanced Ceramics Inc., Cleveland, USA). The experiments were repeated in 2–3 sessions using different tips to check for reproducibility and to avoid experimental artefacts, if any. For analysis purposes, recording of a monolayer image was followed by imaging the graphite substrate underneath under the same experimental conditions, except for increasing the current and lowering the bias. The images were corrected for drift via Scanning Probe Image Processor (SPIP) software (Image Metrology ApS), using the recorded graphite images for calibration purposes, allowing a more accurate unit cell determination. The unit cell parameters were determined by examining at least 4 images and only the average values are reported. The images are Gaussian filtered. The imaging parameters are indicated in the figure caption: tunneling current ( $I_{\text{set}}$ ), and sample bias ( $V_{\text{bias}}$ ). The molecular models were built using Hyperchem 7.0 program.

### UV-vis spectroscopy

All stationary measurements have been recorded using a spectrophotometer (Lambda-950 spectrometer). The spectrometers were corrected for the wavelength dependence of the throughput of the emission monochromator and the sensitivity of the detector. The optical density at the absorption maximum of all solutions was kept below 0.1 in a 1 cm cuvette ( $10^{-5}$  M). The EQE was measured using an integrating sphere (Labsphere) coupled to the abovementioned fluorimeter through optical fibers. Barium sulfate was used during the EQE measurement as fully scattering reference.

### Theoretical methods

#### Density functional theory (DFT) calculations

Density functional theory calculations performed with DMOL3 code available in Biovia's Materials Studio modeling package have been performed to (i) optimize the geometry of **DPP-C12** and **DPP-C12/Pd**, (ii) calculate the torsional profile for the two interring torsions in the conjugated **DPP-C12** core, (iii) compute the ESP charges for all atoms dimers, (iv) calculate the stability and conformation of adsorbed **DPP-C12** and metal coordinated dimers and (v) to validate the choice of the force field used in the classical atomistic models of **DPP-C12** aggregates and monolayers. These DFT calculations were conducted by using the GGA BLYP functional, effective core potentials, DNP+ basis set and the GRIMME dispersion correction.

Modelling supramolecular self-assemblies using quantum chemistry calculations is proving challenging even with modern computers and is therefore best to move towards classical, force-field based, full atomistic models. Having used it to successfully model supramolecular assemblies in the past, we consider the DREIDING force field, improved by using ESP charges from a DFT optimization of a **DPP-C12** molecule in vacuum, as atomic charges.

To validate our choice, we compare the DFT torsional profiles discussed before with those predicted by the force field. Figures S1a and S1b show the comparison between the DREIDING and DFT torsional profiles for the  $\alpha$  and  $\beta$  torsions: while predicting slightly softer torsions, the DREIDING force field can qualitatively reproduce the DFT results.

CCDC 2219946 contains the supplementary crystallographic data for **DPP-C12**. These data can be obtained free of charge from The Cambridge Crystallographic Data Centre via [www.ccdc.cam.ac.uk/structures](http://www.ccdc.cam.ac.uk/structures).



## Supporting Information

Detailed description of materials and methods, crystal structure analysis, modelling, additional STM data, UV-vis spectra are available in the Supporting Information file. Additional references are also cited within the Supporting Information.<sup>[16,22]</sup>

## Acknowledgements

Financial support from the Research Foundation – Flanders (FWO G0 A3220 N) and KU Leuven-Internal Funds (C14/19/079) is acknowledged. This work was in part supported by FWO (G0H2122 N, GF9118 N) and F.R.S.-FNRS under the Excellence of Science EOS program (projects 30489208 and 40007495). The computational resources in Mons are supported by the FNRS “Consortium des Equipements de Calcul Intensif – CECI” program Grant No. 2.5020.11 and by the Walloon Region (ZENOBIE Tier-1 supercomputer, under grant 1117545). T.H. acknowledges the China Scholarship Council (CSC) (No. 202006150018). G.M.V. acknowledges the FWO fellowship award (No. 1269221 N). R.H. acknowledges FWO for financial support through the Wetenschappelijke Onderzoeksgemeenschap (WOG) supramolecular chemistry and materials. K.V.H. thanks the Research Foundation, Flanders (FWO) (project AUGÉ/11/029).

## Conflict of Interests

The authors declare no conflict of interest.

## Data Availability Statement

The data that support the findings of this study are available from the corresponding author upon reasonable request.

**Keywords:** conglomerates · coordination interactions · multiscale molecular modeling · scanning tunneling microscopy · self-assembly

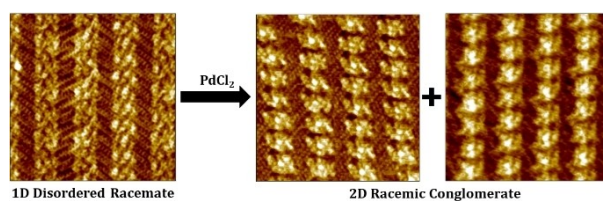
- [1] a) K. S. Mali, N. Pearce, S. De Feyter, N. R. Champness, *Chem. Soc. Rev.* **2017**, *46*, 2520–2542; b) W. Li, J. Zhou, S. Cai, Z. Yu, J. Zhang, N. Fang, T. Li, Y. Wu, T. Chen, X. Xie, H. Ma, K. Yan, N. Dai, X. Wu, H. Zhao, Z. Wang, D. He, L. Pan, Y. Shi, P. Wang, W. Chen, K. Nagashio, X. Duan, X. Wang, *Nat. Electron.* **2019**, *2*, 563–571; c) J. A. Berrocal, G. H. Heideman, B. F. M. de Waal, M. Enache, R. W. A. Havenith, M. Stöhr, E. W. Meijer, B. L. Feringa, *J. Am. Chem. Soc.* **2020**, *142*, 4070–4078.  
 [2] R. Yi, Y. Mao, Y. Shen, L. Chen, *J. Am. Chem. Soc.* **2021**, *143*, 12897–12912.

- [3] B. Daelemans, S. Eyley, C. Marquez, V. Lemmens, D. E. De Vos, W. Thielemans, W. Dehaen, S. De Feyter, *Chem. Sci.* **2022**, *13*, 9035–9046.  
 [4] T. Zhang, Z. Cheng, Y. Wang, Z. Li, C. Wang, Y. Li, Y. Fang, *Nano Lett.* **2010**, *10*, 4738–4741.  
 [5] a) S. De Feyter, F. C. De Schryver, *Chem. Soc. Rev.* **2003**, *32*, 139–150; b) J. A. Theobald, N. S. Oxtoby, M. A. Phillips, N. R. Champness, P. H. Beton, *Nature* **2003**, *424*, 1029; c) A. Ciesielski, P. J. Szabelski, W. Rzyzko, A. Cadeddu, T. R. Cook, P. J. Stang, P. Samorì, *J. Am. Chem. Soc.* **2013**, *135*, 6942–6950.  
 [6] a) A. Cucinotta, C. Kahlfuss, A. Minoia, S. Eyley, K. Zwaenepoel, G. Velpula, W. Thielemans, R. Lazzaroni, V. Bulach, M. W. Hosseini, K. S. Mali, S. De Feyter, *J. Am. Chem. Soc.* **2023**, *145*, 1194–1205; b) M.-A. Carvalho, H. Dekkiche, M. Nagasaki, Y. Kikkawa, R. Ruppert, *J. Am. Chem. Soc.* **2019**, *141*, 10137–10141; c) L. Dong, Z. A. Gao, N. Lin, *Prog. Surf. Sci.* **2016**, *91*, 101–135.  
 [7] R. E. Sikma, K. P. Balto, J. S. Figueroa, S. M. Cohen, *Angew. Chem. Int. Ed.* **2022**, *61*, e202206353.  
 [8] Q. Xue, N. Xue, J. Li, Y. Li, R. Li, Y. Zhang, N. Li, Z. Shen, S. Hou, Y. Wang, *J. Phys. Chem. C* **2020**, *124*, 7790–7796.  
 [9] a) J. R. L. Hong-Cai Zhou, O. M. Yaghi, *Chem. Rev.* **2012**, *112*, 673–674; b) S. L. Griffin, N. R. Champness, *Coord. Chem. Rev.* **2020**, *414*, 213295; c) J. V. Barth, G. Costantini, K. Kern, *Nature* **2005**, *437*, 671–679; d) J. Liu, M. Abel, N. Lin, *J. Phys. Chem. Lett.* **2022**, *13*, 1356–1365.  
 [10] a) P. Messina, A. Dmitriev, N. Lin, H. Spillmann, M. Abel, J. V. Barth, K. Kern, *J. Am. Chem. Soc.* **2002**, *124*, 14000–14001; b) A. Dmitriev, H. Spillmann, M. Lingenfelder, N. Lin, J. V. Barth, K. Kern, *Langmuir* **2004**, *20*, 4799–4801.  
 [11] a) S. De Feyter, M. M. S. Abdel-Mottaleb, N. Schuurmans, B. J. V. Verkuil, J. H. van Esch, B. L. Feringa, F. C. De Schryver, *Chem. Eur. J.* **2004**, *10*, 1124–1132; b) X. Sun, X. Yao, F. Lafolet, G. Lemerrier, J.-C. Lacroix, *J. Phys. Chem. Lett.* **2019**, *10*, 4164–4169.  
 [12] L.-J. Chen, H.-B. Yang, M. Shionoya, *Chem. Soc. Rev.* **2017**, *46*, 2555–2576.  
 [13] a) Z.-Y. Yi, X.-Q. Yang, J.-J. Duan, X. Zhou, T. Chen, D. Wang, L.-J. Wan, *Nat. Commun.* **2022**, *13*, 5850; b) L. Pérez-García, D. B. Amabilino, *Chem. Soc. Rev.* **2002**, *31*, 342–356; c) S. M. Barlow, R. Raval, *Surf. Sci. Rep.* **2003**, *50*, 201–341; d) F. Stevens, D. J. Dyer, D. M. Walba, *Angew. Chem. Int. Ed.* **1996**, *35*, 900–901.  
 [14] Y.-Q. Zhang, T. Lin, B. Cirera, R. Hellwig, C.-A. Palma, Z. Chen, M. Ruben, J. V. Barth, F. Klappenberger, *Angew. Chem. Int. Ed.* **2017**, *56*, 7797–7802.  
 [15] J. A. A. W. Elemans, I. De Cat, H. Xu, S. De Feyter, *Chem. Soc. Rev.* **2009**, *38*, 722–736.  
 [16] R. Hoogenboom, B. C. Moore, U. S. Schubert, *J. Org. Chem.* **2006**, *71*, 4903–4909.  
 [17] G. P. Moss, *Pure Appl. Chem.* **1996**, *68*, 2193–2222.  
 [18] S. Dutta, A. J. Gellman, *Chem. Soc. Rev.* **2017**, *46*, 7787–7839.  
 [19] J. Seibel, M. Parschau, K.-H. Ernst, *J. Phys. Chem. C* **2014**, *118*, 29135–29141.  
 [20] E. C. Constable, C. E. Housecroft, M. Neuburger, S. Reymann, S. Schaffner, *Eur. J. Inorg. Chem.* **2008**, *2008*, 3540–3548.  
 [21] C. Viedma, C. Lennox, L. A. Cuccia, P. Cintas, J. E. Ortiz, *Chem. Commun.* **2020**, *56*, 4547–4550.  
 [22] a) W. A. Butte, F. H. Case, *J. Org. Chem.* **1961**, *26*, 4690–4692; b) Agilent, *Agilent Technologies UK Ltd, Yarnton, Oxfordshire, England* **2014**; c) O. V. Dolomanov, L. J. Bourhis, R. J. Gildea, J. A. K. Howard, H. Puschmann, *J. Appl. Crystallogr.* **2009**, *42*, 339–341; d) G. Sheldrick, *Acta Crystallogr. Sect. A* **2008**, *64*, 112–122; e) R. Hoogenboom, G. Kickelbick, U. S. Schubert, *Eur. J. Org. Chem.* **2003**, *2003*, 4887–4896; f) Y. Fang, M. Cibian, G. S. Hanan, D. F. Perepichka, S. De Feyter, L. A. Cuccia, O. Ivashenko, *Nanoscale* **2018**, *10*, 14993–15002.

Manuscript received: August 4, 2023

Accepted manuscript online: October 15, 2023

Version of record online: ■■, ■■



**Metal-driven transformation** of a 1D disordered racemate self-assembled molecular network into a 2D racemic

conglomerate metal-organic coordinated network at the solution-solid interface is described.

*T. Hu, Dr. A. Minoia, Dr. G. Velpula\*, Prof. Dr. K. Ryskulova, Prof. Dr. K. Van Hecke, Prof. R. Lazzaroni, Dr. K. S. Mali, Prof. Dr. R. Hoogenboom, Prof. S. De Feyter\**

1 – 10

**From One-Dimensional Disordered Racemate to Ordered Racemic Conglomerates through Metal-Coordination-Driven Self-Assembly at the Liquid-Solid Interface**

